Author/s:
Laird, JS;Ravishankar, S;Rietwyk, KJ;Mao, W;Bach, U;Smith, TA

Title:
Intensity Modulated Photocurrent Microspectrosopy for Next Generation Photovoltaics

Date:
2022-01-01

Citation:
Laird, J. S., Ravishankar, S., Rietwyk, K. J., Mao, W., Bach, U. & Smith, T. A. (2022). Intensity Modulated Photocurrent Microspectrosopy for Next Generation Photovoltaics. Small Methods, 6 (9), https://doi.org/10.1002/smtd.202200493.

Persistent Link:
https://hdl.handle.net/11343/320228

small methods
www.small-methods.com

Intensity Modulated Photocurrent Microspectrosopy for Next Generation Photovoltaics

Jamie S. Laird, Sandheep Ravishankar, Kevin J. Rietwyk, Wenxin Mao, Udo Bach, and Trevor A. Smith*

In this report, a large-area laser beam induced current microscope that has been adapted to perform intensity modulated photocurrent spectroscopy (IMPS) in an imaging mode is described. Microscopy-based IMPS method provides a spatial resolution of the frequency domain response of the solar cell, allowing correlation of the optoelectronic response with a particular interface, bulk material, specific transport layer, or transport parameter. The system is applied to study degradation effects in back-contact perovskite cells where it is found to readily differentiate areas based on their markedly different frequency response. Using the diffusion-recombination model, the IMPS response is modeled for a sandwich structure and extended for the special case of lateral diffusion in a back-contact cell. In the low-frequency limit, the model is used to calculate spatial maps of the carrier ambipolar diffusion length. The observed frequency response of IMPS images is then discussed.

1. Introduction

In recent years, metal halide perovskites have attracted enormous attention as they absorb broadly across the solar spectrum and are easily processed into photovoltaic structures using low-cost and low-temperature solution processing.[1] Although champion organic-inorganic perovskite solar cells (PSCs) display photoconversion efficiencies approaching commercial viability,[2,3] they are still inherently unstable under in-operando conditions encountered in the field. Device stability is a key metric and a major concern for large-scale applications.[4–6] The perovskite solar cells yield a complex response to a range of stimuli including light,[7,8] moisture,[9,10] oxygen,[5] temperature, and applied voltage,[11] means qualifying their use over extended periods requires an extensive set of measurements to unravel the complex interplay between the various physical mechanisms determining the overall power conversion efficiency (PCE).[12] Compositional and structural heterogeneity in perovskites is also complex and the resultant interfaces with electron and hole transport layers are a particular concern for stability.[13]

Within this context, small-perturbation techniques such as impedance spectroscopy (IS) and Intensity-modulated photocurrent and photovoltage spectroscopies (IMPS and IMVS respectively) are powerful methods to characterize PSCs and their degradation pathways.[14] The transfer function measured by these methods can be related to an equivalent circuit with the underlying physical processes being lumped as passive electrical components (resistances and capacitances).[15] However, the complex behavior of perovskite devices and their degradation pathways under ambient conditions leads to a strong spatial heterogeneity in the device response. Indeed, this spatial heterogeneity and its dependence on ambient conditions and cell structure may partially explain stark differences in IMPS measurements reported in the literature. Furthermore, Laser beam induced current (LBIC) mapping of OPVs[16–18] and perovskite cells clearly illustrates a strong heterogeneity across a wide range of planar[19–21] and structured devices[22,23] Whilst some of these devices are expected to display large heterogeneity related to structure, it appears that degradation in planar structures with initially near uniform PCE generates a high degree of heterogeneity that further exacerbates with time. For example, Song et al. used LBIC microscopy in an airtight environmental box to follow the heterogeneous degradation and its reversibility in a $MAPbI_3$ (or MAPI) cell under humid conditions.[24] Likewise, noise micro-spectroscopy of degraded MAPI cells also displays a similar strong heterogeneity in cell response over extensive regions of a device. Yao et al. also carried out LBIC imaging of a complete cell under controlled exposure and noted interface degradation, particularly around the device edge.[25]

J. S. Laird, T. A. Smith
Centre of Excellence in Excitons
School of Chemistry
University of Melbourne
Parkville, Victoria 3010, Australia
E-mail: jslaird@unimelb.edu.au

S. Ravishankar
IEK-5 Photovoltaik
Forschungszentrum Jülich
52425 Jülich, Germany

K. J. Rietwyk, W. Mao, U. Bach
Centre of Excellence in Excitons
Chemical Engineering
Monash University
Wellington Road, Clayton, Victoria 3800, Australia

The ORCID identification number(s) for the author(s) of this article can be found under https://doi.org/10.1002/smtd.202200493.

DOI: 10.1002/smtd.202200493

It stands to reason that making bulk IMPS measurements on such heterogeneous systems is not ideal as the measured transfer function Q represents an ensemble average over a sum of spatially variable resistances, not all necessarily the same type. Coupling LBIC microscopy and IMPS seems a particularly powerful union for correlating the locally resolved PCE with a specific interface or transport resistance as typically done with conventional IMPS. Being able to probe and measure the spatial variation of the transfer function across the active area enables a more complete characterization and potential refinement of equivalent circuits used. Furthermore, combining LBIC and IMPS provides an unprecedented ability to investigate PSC stability and degradation under controlled conditions as the ability of IMPS to discriminate between properties of interfaces, absorber, and ionic motion points towards monitoring these quantities spatially as the dynamics of the device evolve. The method may prove critical in better understanding and tracking the decomposition of perovskite cells subjected to a variety of stimuli. In this work, we introduce IMPS microscopy and use it to study the spatial dependence of moisture-related degradation in a back-contact PSC. Using diffusion-recombination theory, we model the IMPS response from which ambipolar diffusion length maps can be extracted from low-frequency experimental data. Apart from this important metric, we illustrate how other frequency bands can be used to study the degradation of a PSC.

2. Background Theory

2.1. Intensity-Modulated Photocurrent Spectroscopy

Frequency domain techniques such as impedance spectroscopy (IS) and intensity-modulated photocurrent or photovoltage spectroscopy (IMPS/IMVS)[14,26,27] rely on measuring the response of a device to a small AC perturbation at a given DC condition. IMPS measures the modulated current response $\tilde{j}_e$ to an applied modulated small perturbation of light intensity (expressed as a current density $\tilde{j}_\phi$) as displayed in **Figure 1**. The modulation is then varied over a range of frequencies resulting in a dispersion relationship or transfer function Q given by: Equation (14)

$$Q(\omega) = \tilde{j}_e / \tilde{j}_\phi \tag{1}$$

The IMPS measurement yields information on the differential external quantum efficiency ($EQE_{PV-\mathrm{diff}}$) of the device through the low-frequency limit of the transfer function, given by:

$$Q(0) = d\bar{j}_e / d\bar{j}_\phi \tag{2}$$

where $\bar{j}_e$ and $\bar{j}_\phi$ are the steady-state photocurrent and photon current, respectively.[28] Note that IMPS can be carried out at any given steady-state condition with any voltage or light intensity. For IMPS, the experimentally measured AC transfer function of the device $Q(\omega)$ is a unit-less complex variable given by:

$$Q(\omega) = Q'(\omega) + iQ''(\omega) \tag{3}$$

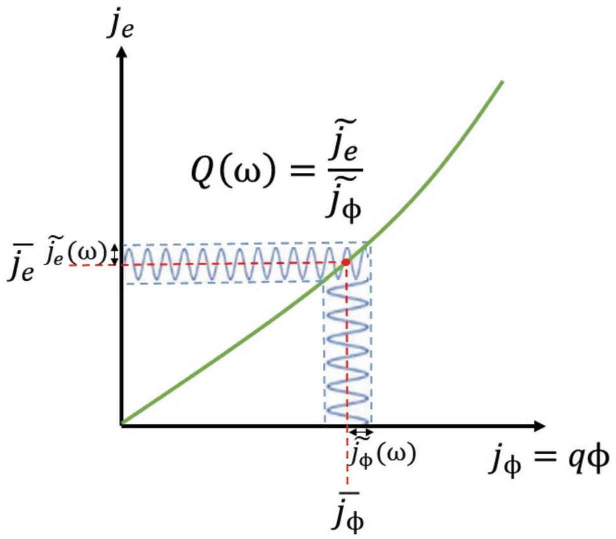

Figure 1. Definition of the IMPS transfer function – ratio of the measured AC current response $\tilde{j}_e$ at various frequencies due to a small perturbation in photon flux $\tilde{\Phi}$ expressed as a current density $\tilde{j}_\phi$, from a given steady state (quantities with overbar).

Since there is no active gain in these devices, Q ranges from 0 to 1, with 1 being the condition for the perfect extraction of generated electron-hole pairs.

IMPS can reveal multiple processes over a broad frequency range, resulting in numerous arcs and loops on a Nyquist plot. By scanning modulation frequency ω, one can decouple kinetics attributed to inherent physical mechanisms by essentially compressing the dynamic range of the measured photocurrent to the associated sub-circuit of the equivalent circuit. In a sense, device components are seen to behave with an "optoelectrical inertia" which responds to a particular frequency band.

The analysis of IMPS spectra of solar cells is usually carried out by either of two methods. The first method employs the use of equivalent circuit (EC) modeling to predict the IMPS response in terms of passive electrical elements (resistances, capacitances, and inductors).[26–28] The advantage of this method is both its simplicity and ease of fitting to EC models whilst allowing extrapolation with other frequency domain techniques to obtain high reliability in the fitted parameters.[28] However, the method is limited to cases where there is no electric field within the absorber and no significant gradient in carrier concentration within, i.e., the diffusion length $L \gg d$ (the layer thickness). It also requires a well-established EC, which is still under debate for PSCs. The second method, and the one employed here, uses the solution of the diffusion-recombination model to obtain characteristic parameters of transport and recombination.[26] This method was applied extensively to study dye-sensitized solar cells[27] and has recently been applied to perovskite solar cells.[29]

2.2. Diffusion-Recombination Transfer Function

As established by Peter et al.,[30] one can derive an analytical model for the transfer function Q of a sandwich-type thin-film

PSC by solving the continuity equation for electronic carrier flow within an absorber layer of thickness d[14] (the mixed ion-electronic conductivity of perovskites is not addressed). With the perovskite material assumed to be approximately intrinsic in nature, carrier transport is ambipolar and the device is in high-level injection conditions ($\overline{n} = \overline{p}$, where $\overline{n}$ and $\overline{p}$ are the steady-state electron and hole concentrations). The continuity equation for electrons in a steady state is given by:

$$\frac{\partial \overline{n}}{\partial t} = \frac{1}{q}\frac{\partial \overline{j}}{\partial x} + \overline{G} - \overline{U} \tag{4}$$

where x is the depth into the absorber and $\overline{G}$ (cm^{-3}s^{-1}) and $\overline{U}$ (cm^{-3}s^{-1}) are the generation and recombination rates respectively and $\overline{j}$ is the electron current density. The electron current density $\overline{j}$ depends on the diffusive flux $\overline{j} = -D\frac{\partial n}{\partial x}$ away from the surface illumination point as dictated by Fick's law. The generation term for the perturbing light source with photon current density $\overline{j_\Phi}$ is given by the Beer-Lambert law:

$$\overline{G} = \frac{\overline{j_\Phi}}{q}\alpha e^{-\alpha x} \tag{5}$$

where α is the absorption coefficient (cm^{-1}). The recombination term is governed by Shockley-Read-Hall (SRH) recombination which is simply (for a deep trap):

$$\overline{U} = \frac{\overline{np} - n_\mathrm{i}^2}{\overline{n}\tau_\mathrm{p} + \overline{p}\tau_\mathrm{n}} \tag{6}$$

where n_i is the intrinsic carrier concentration and τ_n and τ_p are the electron and hole lifetimes respectively.[31] For the typical high-level injection regime studied here, we have $\overline{n} = \overline{p} \gg n_\mathrm{i}$, which yields:

$$\overline{U} = \frac{\overline{n}}{\tau_\mathrm{p} + \tau_\mathrm{n}} \tag{7}$$

Substituting Equations (5), (6), and (7) into Equation (4) and applying a small perturbation in photon current (tilde indicates modulated AC quantities), we obtain:

$$\frac{d\tilde{n}}{dt} = D\frac{d^2\tilde{n}}{dx^2} + \frac{\widetilde{\overline{j_\Phi}}}{q}\alpha e^{-\alpha x} - \frac{\tilde{n}}{\tau_\mathrm{eff}} \tag{8}$$

where the effective lifetime $\tau_\mathrm{eff} = \tau_\mathrm{n} + \tau_\mathrm{p}$. This small AC perturbation is typically a modulated light source and for IMPS imaging is a focused spot scanned across the device and demodulated as a current by a lock-in amplifier. The above equation can be analytically solved in the frequency domain using the following boundary conditions:

$$\frac{\partial \tilde{n}}{\partial x}(0) = 0\left(\text{a perfectly blocking contact}\right) \tag{9}$$

$$\tilde{n}(d) = 0\left(\text{a perfectly extracting contact}\right) \tag{10}$$

The transfer function, as derived by Bou et al.[29] is given by:

$$Q(\omega) = \frac{1 - e^{-\alpha d}\left(\frac{p}{\alpha L_\mathrm{a}}\sinh\left(\frac{pd}{L_\mathrm{a}}\right) + \cosh\left(\frac{pd}{L_\mathrm{a}}\right)\right)}{\left(1 - \left(\frac{p}{\alpha L_\mathrm{a}}\right)^2\right)\cosh\left(\frac{pd}{L_\mathrm{a}}\right)} \tag{11}$$

where $p = \sqrt{1 + i\frac{\omega}{\omega_\mathrm{rec}}}$ and $\omega_\mathrm{rec} = \tau_\mathrm{eff}^{-1}$, $\omega_\mathrm{d} = D_\mathrm{a}/d^2$ is the frequency of diffusion and $\omega_a = D_a\ \alpha^2$ is the frequency of absorption. The parameter d is the absorber thickness, α is the absorption coefficient at wavelength λ, and D_a is the ambipolar diffusivity related to the ambipolar diffusion length L_a via $L_\mathrm{a} = \sqrt{D_\mathrm{a}\tau_\mathrm{eff}}$. For the case where the RC time constant of the cell limits the measurement bandwidth, the measured transfer function is simply:

$$Q_\mathrm{m}(\omega) = Q(\omega) \cdot A(\omega) \tag{12}$$

where the attenuation function A is that of an RC network given by Equation (13):

$$A(\omega) = \frac{1}{1 + i\omega R_s C_g} \tag{13}$$

In our case, IMPS measurements were performed on a back-contact PSC (see Figures 4b,d) with electrode spacing d_elec on the order of 2 µm. The sample was illuminated from the top with a beam spot size larger than d_elec, with photons therefore being absorbed through the thickness of the cell d in the z-direction. We therefore modify the model by assuming all absorbed photons generate (based on the Beer-Lambert law) electron-hole pairs that diffuse to the bottom of the cell ($z = d$), which then must diffuse laterally in the x-direction to the collecting electrodes (determined by the diffusion-recombination model). The modulated generation rate is thus given by:

$$\widetilde{G} = \frac{\widetilde{j_\Phi}}{qd_\mathrm{elec}}\int_0^d \alpha e^{-\alpha z}dz = \frac{\widetilde{j_\Phi}}{qd_\mathrm{elec}}\left(1 - e^{-\alpha d}\right) \tag{14}$$

Substituting Equation (14) for the generation term in Equation 8 and solving the diffusion-recombination model over the electrode spacing d_elec, we obtain:

$$Q = A(\omega)\frac{L_a}{zd_\mathrm{elec}}\left(1 - e^{-\alpha d}\right)\tanh\left(\frac{zd_\mathrm{elec}}{L_a}\right) \tag{15}$$

In the low-frequency limit, $\omega \to 0$, attenuation $A \to 1$ and the transfer function approaches

$$Q(\omega \to 0) = \frac{L_a}{d_\mathrm{elec}}\left(1 - e^{-\alpha d}\right)\tan h\left(\frac{d_\mathrm{elec}}{L_a}\right) \tag{16}$$

Fitting a spline to the function $Q(\omega \to 0)$ as shown in Figure S5, Supporting Information allows one to construct a look-up table to convert low-frequency Q' images into maps of the ambipolar diffusion length, L_a. However, adequate measures need to be taken to discount the influence of ions on the low frequency response, which is discussed in Section 4.3.

2.2.1. Modelling Spectra

Using the diffusion-recombination model, a series of simulations were performed to observe the spectral shapes generated for varying absorption, transport, and recombination frequencies (ω_a, ω_d and ω_{rec} respectively) whilst initially ignoring *RC* attenuation effects (Equation 11). Optical absorption parameters including extinction coefficients k for thin film MAPbI_3 were taken from Leguy et al.[32] which agree with those of Löper.[33] The first set of calculations examines the influence of L_a and λ on Q for a fixed ω_{rec} and absorber thickness of 0.5 µm (derived from cross-sectional SEM measurements introduced later). Results of simulations are displayed in Figures 2 and Figure S1, Supporting Information. As reported by Pockett et al.[36,37] and Bou et al.,[28,38] an arc is formed with increasing frequency with Q eventually moving into the 2nd quadrant beyond some critical high frequency (ω_{crit}) which increases with decreasing α (increasing λ or decreasing ω_a) for all diffusion lengths. For short absorption and L_a larger than d, the characteristic spiral into the third quadrant towards zero at high frequencies is observed, as reported by Bou et al. For $\lambda > 650$ nm or so, Q does not enter the 2nd quadrant since $1/\alpha$ is comparable to or even greater than d. Similar behavior is seen with decreasing L_a (or ω_d) except that $|Q|$ decreases as less charge is extracted ($EQE_{\text{PV - diff}}$ reduces). At longer wavelengths close to 700 nm, the Q curves display the dominance of the diffusion process represented by a straight 45° degree line to zero.[30] Values for ω_{rec}, ω_d and ω_a as defined by equations in the previous section, are given on each curve. Figure S1, Supporting Information, represents the same data with Q' and Q'' plotted versus frequency. Note the difficulty in assigning a dominant process to the peak of the arc when no single frequency (ω_d or ω_{rec}) sits at the peak.

We now examine the influence of *RC* attenuation when the R_sC_g time constant τ_{RC} is similar to or less than diffusion transport and recombination speeds. Figure S2, Supporting Information, summarises results for the case of $\tau_{RC} = 25$ µs (typical R_s values are between 1–5 Ω cm^2 and $C_g \approx 10^{-7}$ F cm^{-2} for a 300 nm-thick PSC) with $\tau_{\text{eff}} = 25$µs, L_a of 20 µm, 1.0 µm, and 0.25 µm (by varying the diffusion coefficient D_a) corresponding to diffusion frequencies ω_d greater than 50 MHz, 160 kHz, and 10 kHz, respectively. The spectra are very similar to those in **Figure 2** (simulations without attenuation effects) irrespective of whether ω_d is much smaller or greater than $1/\tau_{\text{RC}}$, making it difficult to separate *RC* effects from diffusion-recombination behavior. For longer diffusion lengths, the *RC* time constant dominates the Q-plot and as ω_d increases, the level of an excursion into the 2nd and 3rd quadrant reduces with the 3rd quadrant contribution disappearing faster than the 2nd. Only short diffusion lengths similar in magnitude to the thickness display a characteristic dip into the 3rd quadrant as seen in Figure S2b, Supporting Information, where some information can potentially be extracted from Q-plots if R_sC_g can be independently measured and fitted. However, it is well known that PSCs possess diffusion lengths of the order of several microns[37,38] indicating that this characteristic situation is unlikely for a thin-film PSC. Furthermore, we note that IMPS measurement systems possess upper limits to the measurement frequency usually between 200–300 kHz, making it more difficult to rely on the validity of the high-frequency data. We conclude that it is very difficult to identify situations where the diffusion-recombination response can be clearly differentiated from *RC* attenuation effects for a thin-film PSC. This mainly stems from the fact that in sandwich style, the thin-film cells have a large geometric capacitance, which lowers the attenuation frequency ω_{att} ($\omega_{\text{att}} = 1/R_\text{s}C_\text{g}$) to within the experimental range of frequencies. Therefore, a useful method to circumvent this problem is to measure the response of a PSC in a lateral configuration, where the electrodes are spaced in the order of micrometers, ensuring that the geometric capacitance is much smaller and hence, ω_{att} is large enough to not interfere with the measured response. Indeed, this is the strategy taken here and is further discussed in Section 3.1.

2.3. IMPS Imaging and Laser Beam Induced Current Microscopy

Performing IMPS microscopy relies on adapting already existing methods such as optical or laser beam induced current (LBIC) microscopy. LBIC and OBIC are both widely employed throughout the semiconductor industry.[39–45] The PV mapper illustrated here differs from a typical LBIC setup in that it measures a photoimpedance vector at each pixel. Unlike LBIC, which typically uses a DC or even pulsed beam,[44] here the illumination $I(x, y, t)$ has two terms as shown in Equation (17). The first term I_o is widefield illumination of the sample typically set to ≈1 sun and $\delta(x, y)$ is the beam spot profile scanned across the device with a rate dependent on the time for demodulation at each frequency, f (in Hz). The overall equation for the intensity at any point in time is:

$$I(x, y, t) = I_o + \delta(x, y)\sin(2\pi f) \tag{17}$$

Another point where this technique differs from typical LBIC is the background illumination I_o which light biases the device splitting the quasi-Fermi levels and setting V_{oc} as well as other important injection-dependent parameters such as carrier densities and effective lifetimes. A simple diagram for the IMPS imaging setup is given in **Figure 3** and consists of a large area galvanometer scanner for cells up to ≈10 × 10 cm. A large area format was chosen for this work as the aim is to eventually scan larger cells to investigate scaling issues. However, the same setup is also being installed on a confocal microscope for high-resolution studies. In addition, it includes a temperature stage (not used here) and a *J–V* measurement system. Software for the system includes the capability to batch jobs to fully automate parameter space investigations. For example, IMPS image versus frequency as a function of time with *J–V* (light and dark) can be collected after each frequency (not performed here).

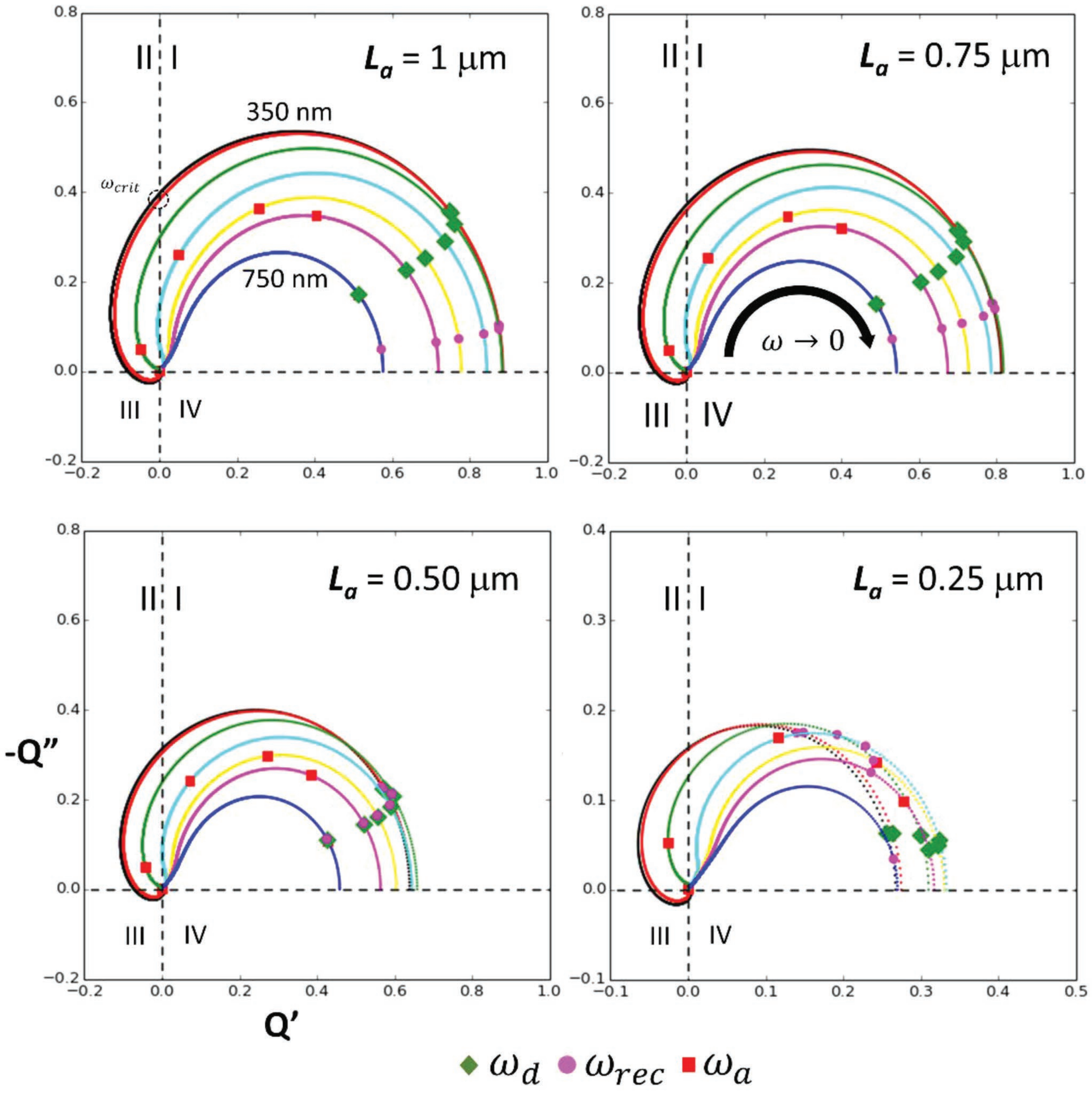

Figure 2. Nyquist Q plots versus λ from 350 nm (black) to 750 nm (blue) for diffusion lengths ranging from 1 µm to 0.25 µm with a 0.5 µm thick absorbing layer. Also shown are the respective values of ω_{rec}, ω_d and ω_a. Shown in the top right figure is the direction of the Q curve as $\omega \rightarrow 0$. A τ_{eff} of 25 µs was assumed.

3. Experimental Section

3.1. Data Collected on Back Contact Sample

A brief example of the method applied to a novel back-contact PSC is given with an emphasis on the technique's imaging aspects. With traditional sandwich structures approaching their PCE limits, new architectures are required to further improve the PCE of perovskite solar cells.[46] The back-contact cell has the typical sandwich structure replaced by alternately interdigitated contacts. The architecture of the cell compared to a standard *p-i-n* or inverted structure is shown in **Figure 4**a-c. Note the cell does have some encapsulation around the periphery to prolong its lifetime with respect to moisture.[47] SEM imaging of the device cross-section indicated an electrode gap d_{elec} of 2 µm, finger thickness of ≈200 nm and a MAPI absorber thickness of ≈500 nm as shown in Figure 4d.[22] The size of each cell is 2 × 2 (mm)^2. Details on fabrication including the use of ZnO

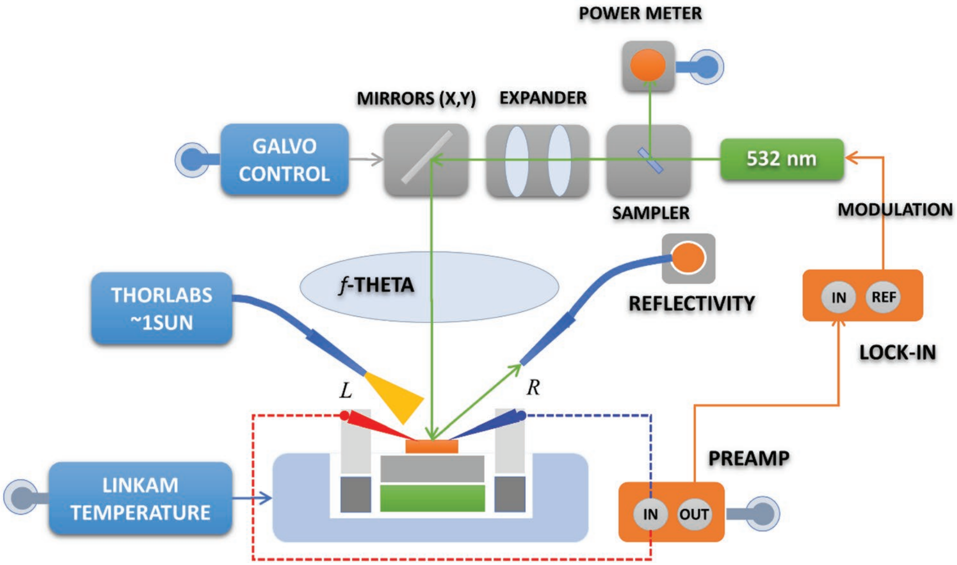

Figure 3. A simplified schematic of the LBIC system used for IMPS imaging of perovskite cells. The system is arranged in the vertical configuration shown with the laser source (532 nm) being scanned across the solar cell using a galvanometric scanning mirror prior to which the beam power is measured. Contacts to transport layers can be made with micromanipulator probes (left and right). The differential current is preamplified and fed into a lock-in-amplifier. The same lock-in provides a reference modulation signal which controls the laser output. A temperature stage also exists but is not used here. A reflectivity probe can also collect an image of the surface for alignment and dust inspection (not used here).

and NiOx as the electron selective layer (ESL) and hole selective layer (HSL), respectively are detailed by Jumabekov et al.[22] The typical PCE for this architecture is ≈3.5%.

The main advantage of this architecture for IMPS measurements is that top illumination (beam spot size larger than electrode spacing d_{elec}) ensures electrons and holes diffuse vertically

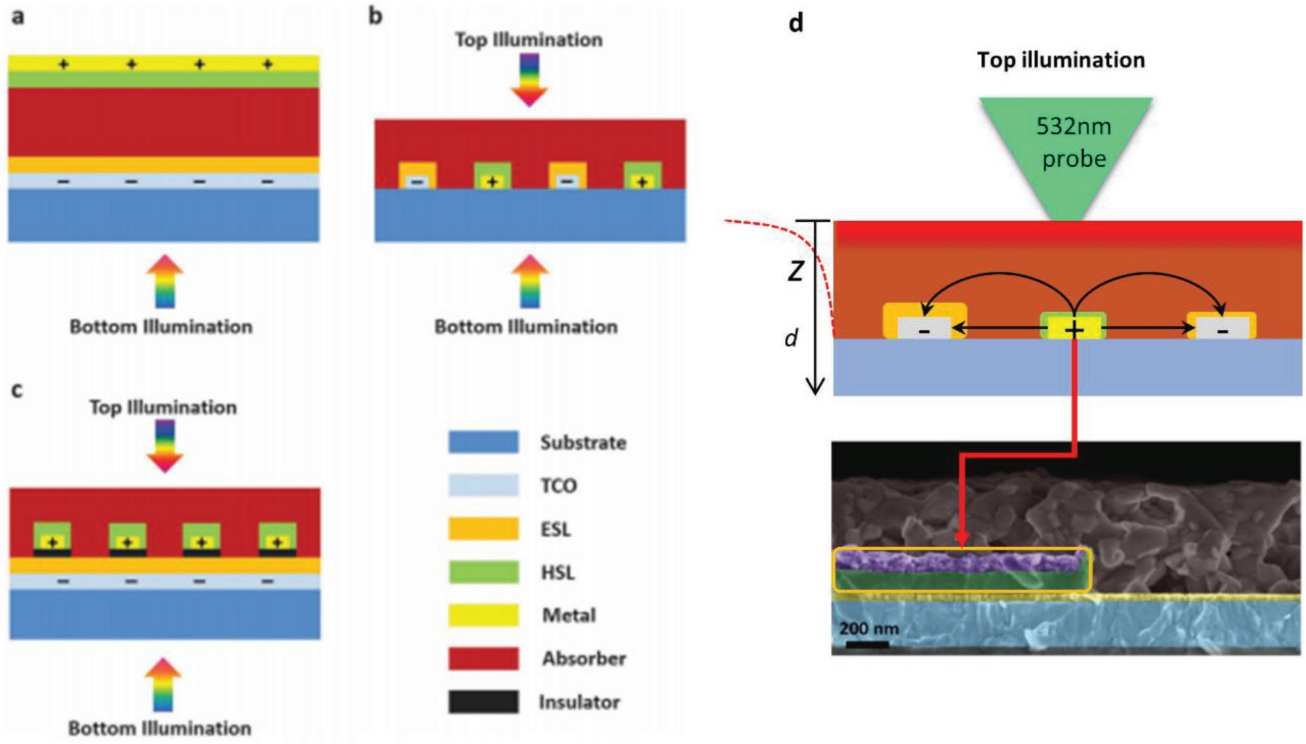

Figure 4. Architectural schematic of the back-contact device b,c) compared to its predecessor designs (a) and (c). d) Laser absorption causes a sharp distribution of carriers near the surface of the device. Carriers first diffuse vertically down, followed by lateral diffusion towards their respective collecting contacts. Bottom SEM image taken with permission from Jumabekov et al.[22] Royal Society of Chemistry.

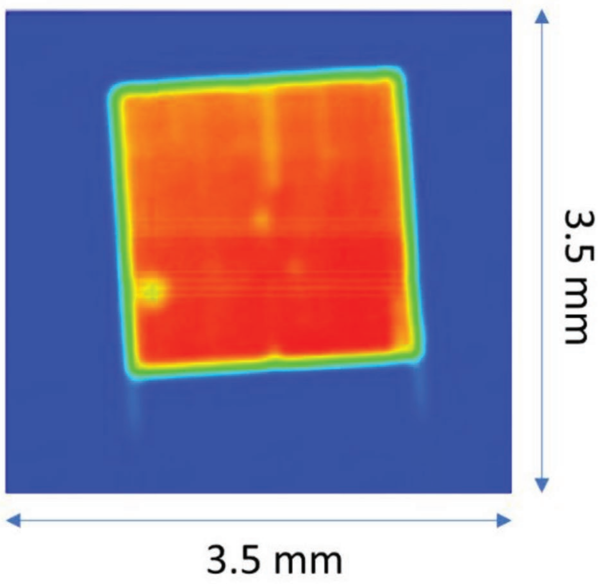

Figure 5. A 3.5 × 3.5 mm top illumination IMPS map taken at 1 kHz on the fresh cell with a V_{oc} of ≈0.95 V.

through the 500 nm thick absorber, followed by lateral diffusion to their respective contacts, which are laterally spaced 2 µm apart. This gap and electrode orientation ensures the *RC* attenuation frequency ω_{att} of a fresh device remains high enough (for $d_{elec} = 2$ µm, assuming $R_s = 5\ \Omega\text{cm}^2$ and relative permittivity of 30, $\omega_{att} \approx 15$ MHz) to not significantly influence the measured spectra (between 125 Hz and 25 kHz). *J*–*V* measurements on a fresh device indicated an open circuit voltage of ≈0.95 V at a light bias of ≈1 sun. Measurements of V_{oc} versus time on a similar batch of samples indicate the open-circuit voltage stabilizes within several seconds of DC illumination even after the onset of degradation. Using the same device, a 532 nm beam with relatively low power (≈200 µW) was raster scanned across the cell and an IMPS image was recorded at 1 kHz as shown in **Figure 5**. Low powers were employed to keep the signal perturbation as small as possible and to avoid other phases appearing (Barbe et al. noted the generation of PbI_2 islands in a MAPI device for irradiation powers in the mW regime[48]). The same study reported a slight increase in photocurrent for low power irradiations like that performed here.

The device was then stored in the dark in a low humidity cabinet for about 2 weeks after which it was mounted on the LBIC microscope with humidity ≈50% for ≈2 weeks. According to Song et al., the hydration of the MAPI layer is probably irreversible for this length of exposure.[24] Measurements of V_{oc} versus time on a similar batch of samples indicate the open-circuit voltage stabilizes within several seconds of DC illumination even after degradation dropped it to less than half its original value. A series of 2.5 × 2.5 $(\text{mm})^2$ scans with modulation frequency varied from 125 Hz to 25 kHz was then performed with the resultant $|Q_{xy}|$ images displayed in **Figure 6** (calculated by the formula given in the figure). What is immediately apparent is that heterogeneity in the degraded response occurs over length scales well beyond that of the electrode patterning and up to a significant fraction of the cell dimension highlighting the need for large area mapping. Note the $Q > 1$ values at low frequency (<1 kHz) are related to 10%–20% error in the extrapolated laser power at low modulation rates. They do not affect interpretation or measurements at higher frequencies. It is worth noting the caveat of rapid large area scanning is the loss in spatial resolution to ≈10 µm or so for the system devised here. The broader laser profile used here ensures a near uniform *e*-*h* pair generation profile across the electrode gap. Image *z*-values are *Q* values determined by the lock-in response and that of a calibrated Si photodetector (A/W) (30 µA mW^{-1} at 532 nm).

4. Results and Discussion

4.1. Results

Analysis of IMPS images generally follows similar principles to bulk IMPS spectra where data is plotted on a complex *Q* plane and results in several arcs, generally in the upper 1st or 2nd quadrant.[14] Here, however, we extend that analysis by extracting information from either the entire cell or specific regions of interest (ROI). The response of the entire cell is given in **Figure 7** and surprisingly covers all 4 quadrants starting in the 3rd quadrant at 125 Hz and moving counterclockwise with increasing modulation into the 1st and finally 2nd quadrant at high frequency. Each point in these plots represents the IMPS response at a single pixel within the chosen ROI for a specific modulation frequency. The sheer number of pixels in the image results in a distribution or band clumped at each frequency.

Each frequency displays a unique arc-like distribution spanning a large range in |*Q*| and phase values related predominantly with the frequency dependence of the underlying physical mechanism. Under these conditions, it clearly makes more sense to use an ROI to section the frequency analysis into specific regions to better understand the behavior of the local transfer function $Q_{xy}(\omega)$. For this purpose, we define numerous bright (high |*Q*|) and dark (low |*Q*|) regions representative of the heterogeneity in the cell response for frequencies above 2 kHz. A polygon and circle represent the typical bright response whereas a triangle, rectangle and oval represent the dark response, with the triangle having the strongest negative behavior as seen from the 25 kHz image in the top section of Figure 11. Below 1 kHz, the images tend to display large negative photocurrents (*Q*' is negative) and significantly higher levels of noise related to ionic polarization as illustrated by the 125 Hz image. The low-frequency behavior of the PSC has been found to be strongly affected by time drift in its response, for which correction procedures have been suggested.[49]

Note that the response starts in the 4th quadrant at frequencies below 1 kHz and ends in the 2nd or 3rd quadrant at high frequencies >10 kHz. Large responses in the 3rd quadrant at mid frequencies seem related to “dark” regions bounded by the dark contours seen in the 4–5 kHz range. Shown in the 25 kHz image are the assorted shapes representing areas (bright and dark) where further extractions were made and displayed in **Figure 8**. These defined shapes were simply chosen by eye

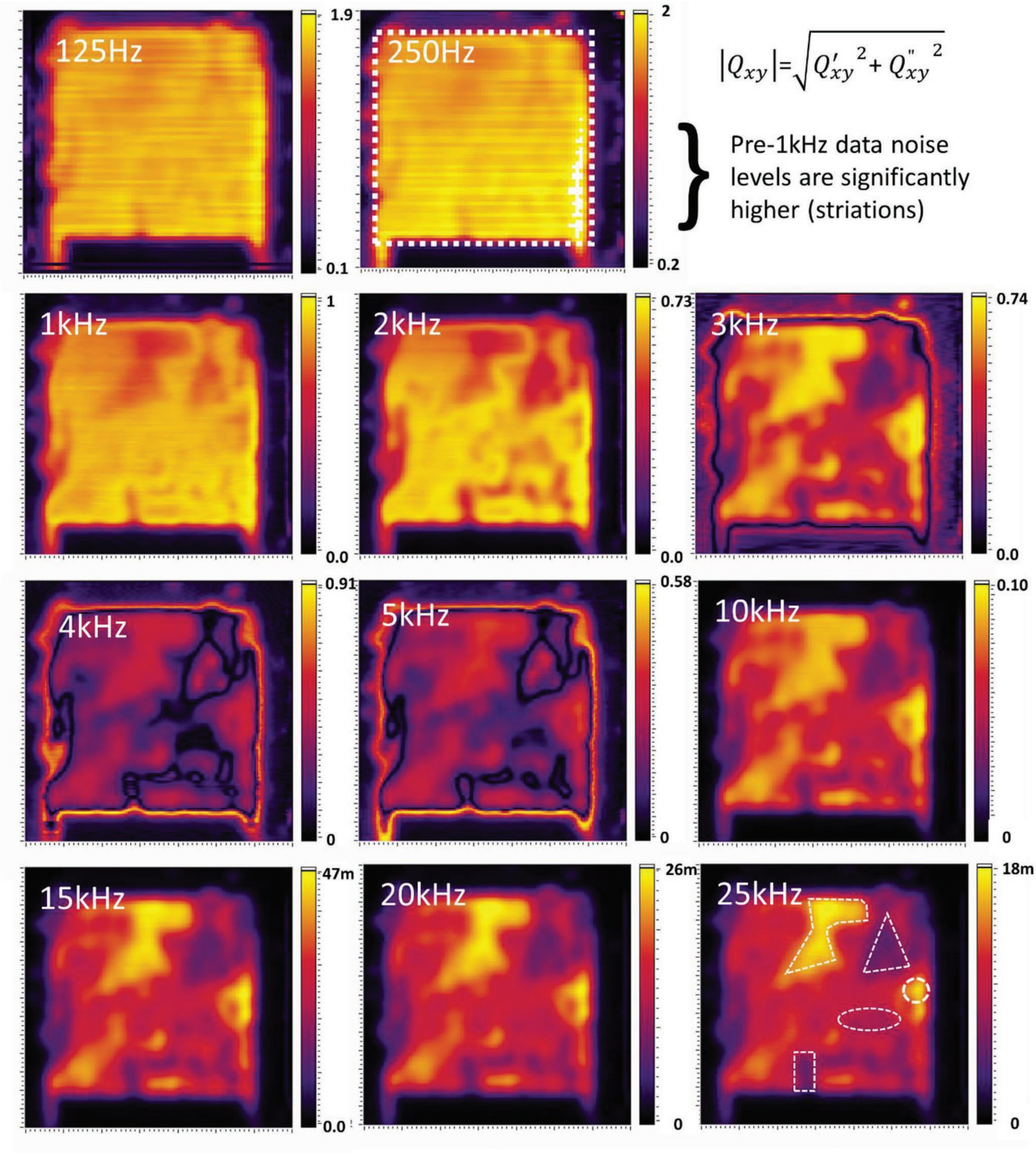

$$|Q_{xy}|=\sqrt{{Q'_{xy}}^{2}+{Q''_{xy}}^{2}}$$

Pre-1kHz data noise levels are significantly higher (striations)

Figure 6. |*Q*| images (2.5 × 2.5 mm) taken on the back-contact cell from 125 Hz to 25 kHz after 1–2 weeks exposure to ambient conditions (≈50% humidity). The large square shown at 250 Hz is the shape for data representing the entire cell shown in Figure 7. The shapes shown at 25 kHz are used for local extractions in bright and dark areas. Note the dark contours displayed in the 3–5 kHz frequency band.

based on apparent uniformity in that region and not due to a specific range of the IMPS values. On the right side are loops extracted from the polygon/circle whereas the left side displays results from the rectangle/oval (the triangle displays similar features).

The bright and dark regions show the same general trends as IMPS in thin-film PSCs, where an arc is observed in the Q plane, with larger Q' values and hence higher photocurrents at lower frequencies, while the Q' value and hence photocurrent drops at higher frequencies. However, the Q plots in

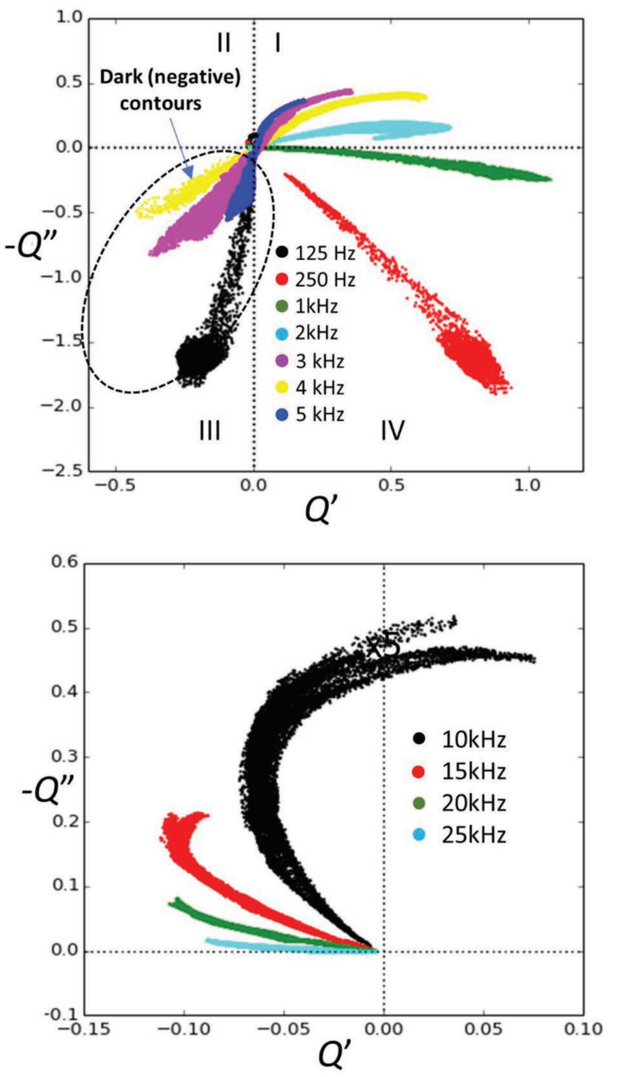

Figure 7. (Top) $-Q''$ versus Q' plots versus frequency from 125 Hz to 5 kHz for the entire device (excluding the surrounding area as shown by a dotted square in the 250 Hz image in Figure 6). (Bottom) The same plot continued from 10 to 25 kHz. Unlike bulk IMPS, here single frequencies display entire arc distributions with each point being a pixel value from an image. Note the large negative photocurrents with large phase changes occur in the dark contours.

the dark areas are noticeably different with large excursions into the 3rd quadrant before returning to the 2nd quadrant. Plots of Q' and $-Q''$ versus frequency for the same regions are shown in **Figure 9**. Finally, **Figures 10**, and **11** display the Q'_{xy} images and the total Q' histograms as a function of frequency. These histograms are essentially log plots of the frequency of occurrence of a particular Q' within an ROI versus Q' itself (m on the x-axis refers to the milli range). Here they are indicative of the distribution of Q' and its sign within an ROI as a function of modulation frequency. The black points represent the entire cell whereas the red ones are the shape ROI which in this case was the polygon. The blue arrow simply points to zero. Importantly, in the 3–5 kHz frequency regime, the amplitudes of some Q' pixels are negative and similar in magnitude to positive values in other parts of the cell. The dashed lines in all Q plots are spline fits to the separate $Q'(\omega)$ and $Q''(\omega)$ plots projected back onto the Nyquist plane.

4.2. Statistics

Very few statistical methods are employed in this paper, but some comments are necessary.

1. All images in this work were generated using raw experimental data without any smoothing or image processing to reduce noise. Rather, longer pixel dwell times were used to reduce noise thereby producing relatively noise-free images.
2. When referencing values generated within specific regions, the distribution of values from the region in question is generally averaged or median filtered to obtain a representative of the region as well as its spread (variance) which are not used in this paper. Unless stated otherwise, an average filter is used.
3. Histogram plots extracted from specific shapes are again displayed as raw data and do not pass-through filters of any type.
4. For some curves presented here, a cubic spline is also generated simply as a reasonable line for the eye to follow. Cubic splines are only used to extract quantitative numbers for the case of extracting the ambipolar diffusion length across an image.

4.3. Discussion

Large heterogeneities in the degraded cell response seem to stem from the outer rims and move into the device which seems consistent with the fact that $MAPbI_3$, being hygroscopic, absorbs moisture from the device periphery once the encapsulation fails. Initially, we focus on the low-frequency response where diffusion length maps can be estimated. The more complex higher frequency response is then discussed for the bright (high $|Q|$) and dark (low $|Q|$) regions represented by the assorted shapes shown in Figure 6. Whilst we term regions bright and dark, this does not refer to a high or low PCE but simply a positive or negative real part of the transfer function Q for a specific frequency or band. Note this discussion is designed to illustrate the advantages of an imaging IMPS and a more detailed discussion will ensue in time as the technique is refined with respect to some of the complex behavior outlined below. Some complications in the method and interpretation of results such as non-uniform beam excitation and light-induced degradation are briefly discussed in Section 3 of the SI.

As outlined in Section 2.2, it is possible to extract a map of the ambipolar diffusion length using the low-frequency limit of $Q(\omega)$ where the attenuation factor approaches unity. However, IMPS models presented earlier are based on electronic carrier transport and do not account for ionic motion which is known to strongly affect the low frequency response.[50] Compared to other dynamical processes, ion migration can be an extremely slow process typically occurring from ms to seconds.[51,52] Calculating diffusion length maps must therefore choose a frequency which is fast enough to avoid ionic

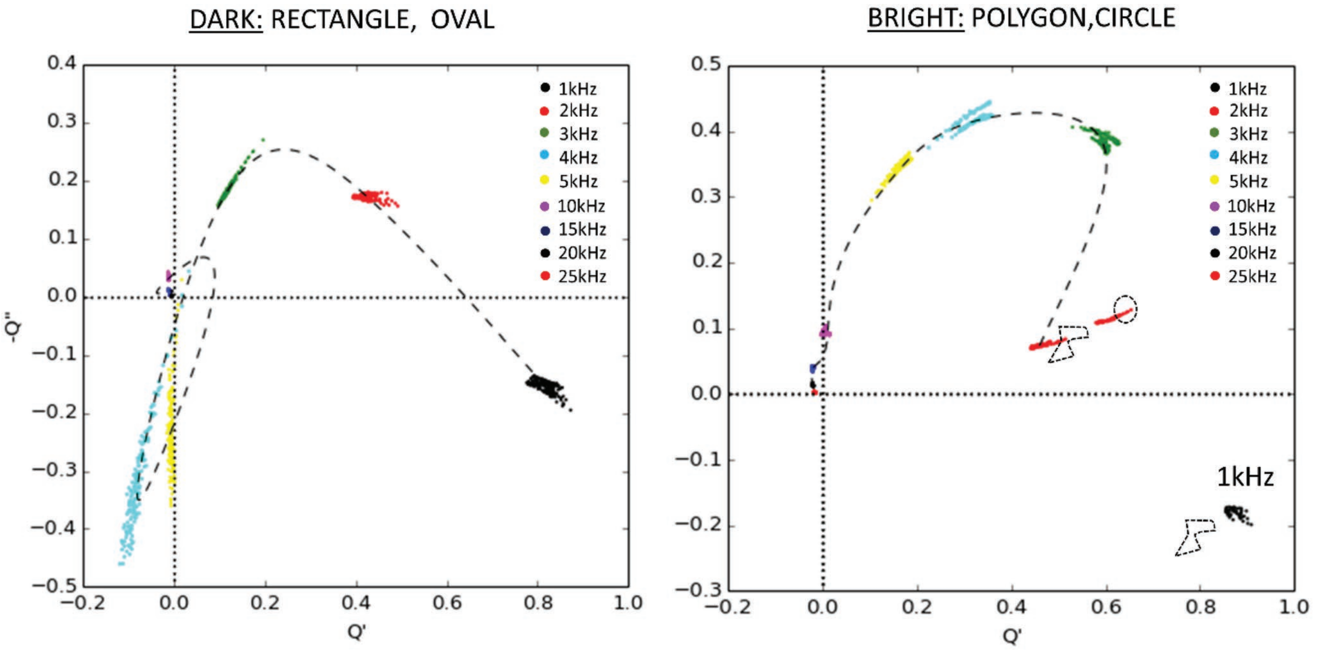

Figure 8. (Left) *Q* response in the rectangle/oval dark region in figure 6 has a loop which starts in the 4th quadrant at low frequency, moves through a peak between 2 and 3 kHz and then moves strongly into the 3rd quadrant. After this, it follows a similar behavior as the bright region and finishes in the 2nd quadrant. Note the cubic spline over emphasizes the loopback. (Right) *Q* response in the polygon/circle regions follows a more typical IMPS curve, starting in the 4th quadrant below 1 kHz before moving into the 1st and finishing in the 2nd quadrant.

movement but slow enough to avoid *RC* attenuation. In this context, image noise represents a useful proxy for detecting the transition frequency above which ionic movement does not contribute to the IMPS response. Impedance analysis of PSCs commonly employs an equivalent circuit model which includes a low-frequency interfacial capacitance C_s related to an electronic accumulation layer at the surface, which is also influenced by ionic accumulation and is highly dependent on light intensity and is orders of magnitude larger than the bulk geometric capacitance, C_g.[53] This interfacial capacitance dominates at frequencies below 1 kHz or so resulting in a large $1/f$ contribution to the photocurrent noise.[54,55] Here, image noise was indeed found to markedly increase below 1 kHz as seen by the horizontal striations in photocurrent shown in Figure 6. At 1 kHz, the noise is negligible and therefore assumed to be the lowest frequency beyond which the IMPS response is dominated by electronic carriers. In addition, the lateral architecture of our back-contact PSC ensures that *RC* attenuation effects are negligible at 1 kHz ($\omega_{\text{att}} \approx 15$ MHz, as mentioned in Section 3.1). Thus, the IMPS response of our cells at 1 kHz was considered the low-frequency limit of the modified diffusion-recombination model (Equation 16). Using the measured absorber thickness of 0.5 µm, electrode spacing of 2 µm and absorption length $1/\alpha$ of 0.105 µm (at 532 nm), the 1 kHz image was converted to a map of the ambipolar diffusion length, L_a as displayed in the left panel in **Figure 12**. The top half of the device has clearly degraded faster than the bottom with all shapes given in Figure 6 exhibiting degraded L_a compared to the relatively undamaged region near the lower right edge. It is difficult to postulate as to why the bottom right edge seems relatively protected except to speculate that encapsulation did not fail in this region like it did in the rest. The panel on the right in Figure 12 is a histogram plot indicating the total scan (black) as well as a representative portion of the background (BACK) which is green. A square around the cell is blue. The assorted ROIs defined in Figure 7 are represented by the polygon plot (red). The distribution of diffusion lengths within the cell is between 600 nm to 1.5 µm, the highest values of which are similar to the electrode spacing of 2 µm. Remember that this analysis assumes the charge is perfectly extracted at the collecting contact ($\tilde{n}(d_{\text{elec}}) = 0$). For PSCs, this assumption is not completely valid as the low-conductivity transport layers have been shown to lead to significant collection losses and influence the impedance and capacitance response significantly.[56] In the absence of an advanced model that accounts for the influence of the selective contacts, the calculated ambipolar diffusion length map is a lower limit to the actual diffusion length in the PSC.

Now we consider the mid-to-high frequency data beyond 2 kHz. Figure 8 shows the IMPS spectra of the bright and dark regions of the cell. As mentioned earlier, the dark regions cross into the second quadrant at high frequencies before approaching the origin, while the bright regions remain in the first quadrant. Furthermore, the data produces an arc with a peak in *Q'* with corresponding time constant ranging between 0.27 and 0.39 ms. If diffusion did dominate the arc, the resultant ω_d would be orders of magnitude lower than expected unless L_{a} was extremely small or the lifetime τ_{eff} unrealistically long ($\omega_{\text{d}} = (L_{\text{a}}/\sqrt{\tau_{\text{eff}}}\,d)^2$). For example, an electrode spacing of 2 µm and ω_{d} of 3.6 kHz would result in a diffusion coefficient of 14×10^{-5} cm^2/s, which is orders of magnitude smaller than those recently reported in the literature.[29,57]. However, the simulations in Figure S2a, Supporting Information, of the diffusion-recombination model including *RC* attenuation show a

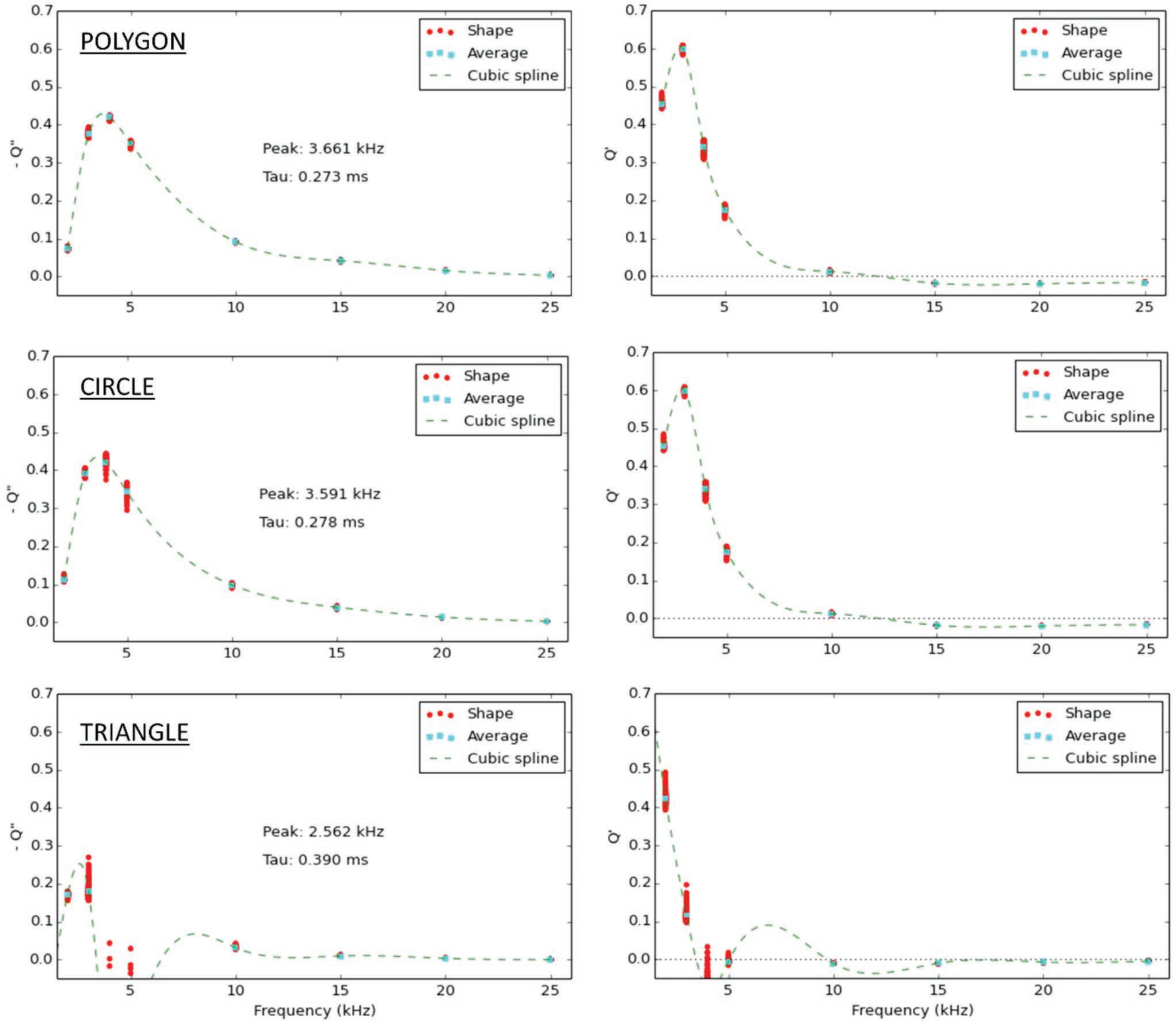

Figure 9. Q' and Q'' versus frequency for the bottom square and right oval regions in the figure. The distribution within the shape is a red circle whereas its average is cyan. A cubic spline fit to the data is used to extract the peak frequency and time constant, τ with values of 0.278 and 0.281 ms.

similarity to the measured data, where larger diffusion lengths (which correspond to bright regions) do not cross into the second quadrant at high frequencies while smaller diffusion lengths (which correspond to darker regions) cross over into the second quadrant (simulations without RC attenuation show the opposite trend with diffusion length, see Figure 2). Thus, we speculate that the high-frequency data is influenced to a degree by RC attenuation effects, especially in the darker regions due to an increase in the series resistance R_S upon degradation.

Clearly, the most troublesome data to explain is the presence of a bimodal distribution in negative values. The first distribution occurring from 3–5 kHz predominantly sits within the 3rd quadrant with large negative amplitudes as seen in Figures 7, 8, and 11. The second distribution has much smaller values and seems associated with transitions into the 2nd quadrant at frequencies beyond 5 kHz as shown by the sequence of histograms in Figure 11. This distribution is not unexpected at higher frequencies as predicted by the IMPS model presented earlier. Indeed, the model also predicts eventual movement into the 3rd quadrant but at much higher frequencies than those applied here. Critically though, the resultant $|Q|$ values beyond these transitions are very small (see Figure 2 for example), meaning they cannot explain the first distribution. The exact nature of the first distribution seems intricately linked to the degradation-related dark contours including those around the edge in Figure 6. An example Q curve for such a dark region is typified by the curve in the rectangle ROI seen in Figure 8 (left). The large excursion into the 3rd quadrant is unlikely to be related to ionic movement and appears confined to very specific regions of the device. Indeed, they appear to follow almost corrosive-like pathways emanating from the device periphery starting at 3 kHz.

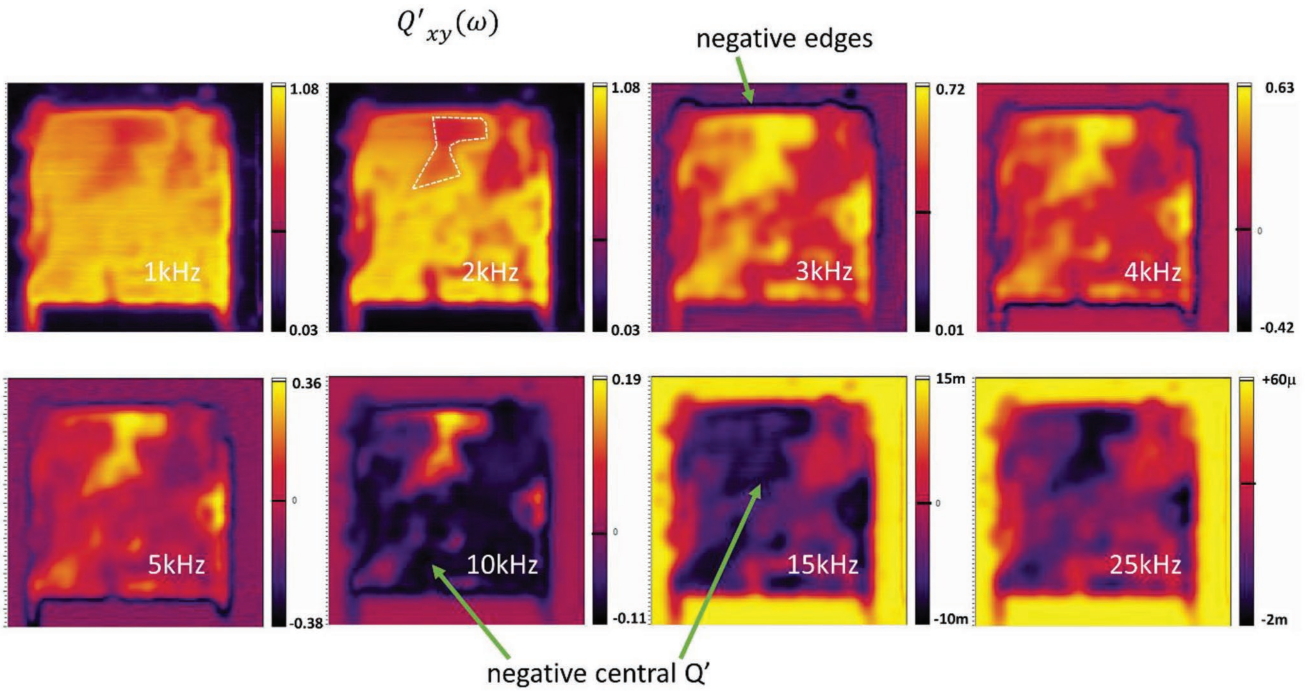

Figure 10. *Q*' images spanning 1–25 kHz illustrate the gradual change into negative photocurrent territory starting around the edges at 3 kHz.

5. Conclusion

In summary, we have presented a novel implementation of IMPS imaging which we envisage becoming a versatile method for investigating degradation and stability in next-generation photovoltaic cells. This method allows spatial resolution of the IMPS response of a solar cell and was tested on a moisture degraded back-contact perovskite solar cell. The lateral structure of the back-contact perovskite solar cell ensures that *RC* attenuation effects are minimized, allowing for accurate analysis of the IMPS response as compared to its thin-film sandwich-type counterparts. Using the diffusion-recombination

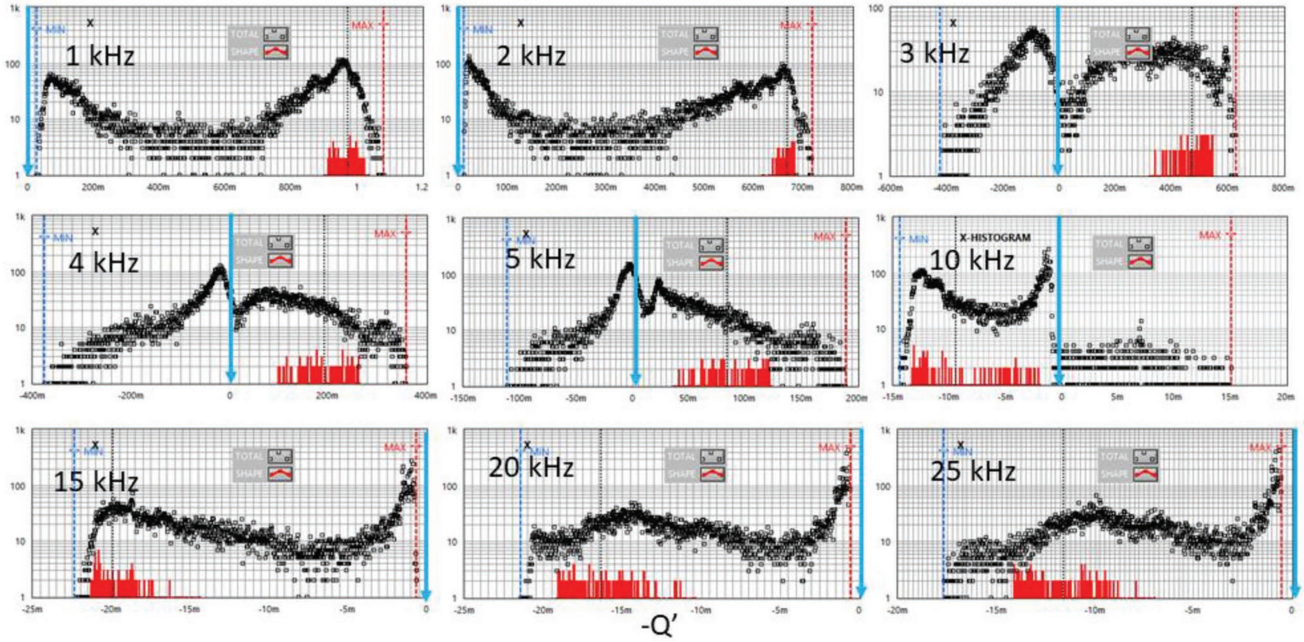

Figure 11. Total *Q*' log scale histograms spanning 1–25 kHz illustrate a general move into negative photocurrent territory starting around the edges at 3 kHz. The blue line displays the zero point in each spectrum. Between 3 and 5 kHz, the negative currents are very large (3rd quadrant) and similar in magnitude to the positive contributions. Beyond this, they decrease in amplitude as they move into the 2nd quadrant. The signal is completely negative above 15 kHz.

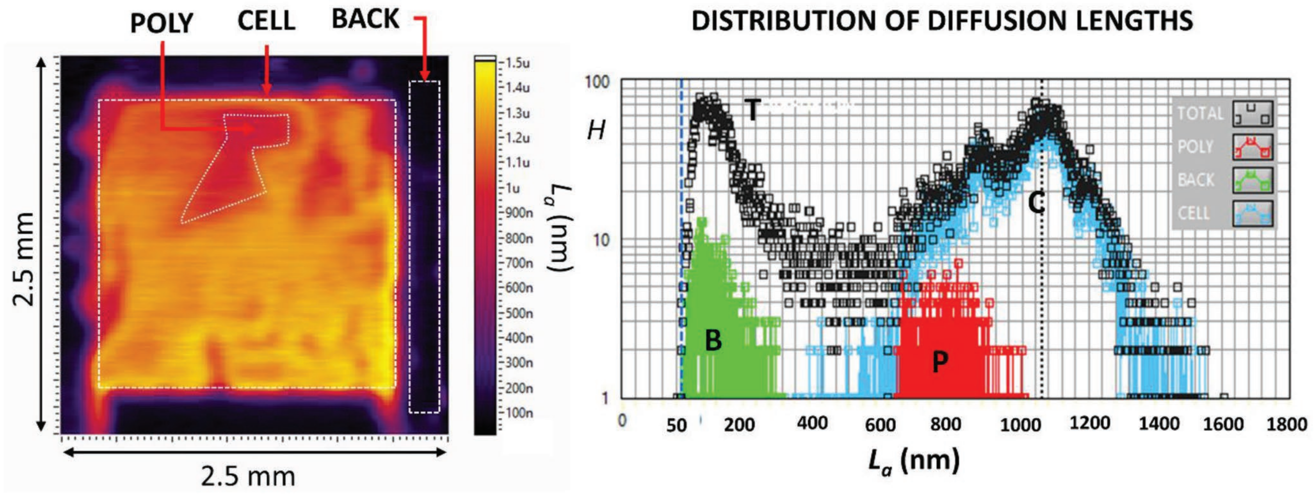

Figure 12. Map of lower limit of ambipolar diffusion length of the perovskite layer generated from the 1 kHz Q' map (ranges from ≈100 nm to 1.5 µm). The device response as seen from the cell histogram (blue) ranges from ≈800 nm in the dark regions such as the polygon (red) region used earlier through to 1500 nm in the bottom right. The background signal provides a false measurement above the noise threshold of 50–300 nm or so as seen by the green plot. "P", "C", "B" and "T" correspond to POLY, CELL, BACK and TOTAL SCAN, respectively.

model, spatially resolved ambipolar diffusion length maps were obtained indicating regions of severe to moderate levels of degradation. Ambipolar diffusion maps at low frequency and corrosive-like morphology in the IMPS maps at higher frequencies illustrate the level of heterogeneity that bulk IMPS would simply average over. For thin film PSCs where the spectra are likely dominated by RC attenuation, spatial variation in series resistance can be measured by this method. In summary, the technique is able to separate the various components leading to cell degradation thereby providing a unique tool for better understanding cell degradation at scales of important for commercial applications.

Supporting Information

Supporting Information is available from the Wiley Online Library or from the author.

Acknowledgements

All authors except S.R acknowledge the Centre of Excellence in Exciton Science funded by the Australian Research Council (ARC) (project No CE170100026). S.R. acknowledges the German Research Foundation (DFG) for support through a Walter-Benjamin fellowship (Project No. 462572437).

Open access publishing facilitated by The University of Melbourne, as part of the Wiley - The University of Melbourne agreement via the Council of Australian University Librarians.

Conflict of Interest

The authors declare no conflict of interest.

Data Availability Statement

The data that support the findings of this study are available from the corresponding author upon reasonable request.

Keywords

intensity modulated photocurrent spectroscopy, laser beam induced current, metal halide perovskites, perovskite solar cells, photocurrent mapping, power conversion efficiency

Received: April 17, 2022
Revised: July 3, 2022
Published online: August 16, 2022

---

[1] A. Kojima, K. Teshima, Y. Shirai, T. Miyasaka, *J. Am. Chem. Soc.* **2009**, *131*, 6050.
[2] H. J. Snaith, *J. Phys. Chem. Lett.* **2013**, *4*, 3623.
[3] M. A. Green, A. Ho-Baillie, H. J. Snaith, *Nat. Photonics* **2014**, *8*, 506.
[4] S. Castro-Hermosa, S. K. Yadav, L. Vesce, A. Guidobaldi, A. Reale, A. di Carlo, T. M. Brown, *J. Phys. D: Appl. Phys.* **2017**, *50*, 033001.
[5] T. A. Berhe, W. N. Su, C. H. Chen, C. J. Pan, J. H. Cheng, H. M. Chen, M. C. Tsai, L. Y. Chen, A. A. Dubale, B. J. Hwang, *Energy Environ. Sci.* **2016**, *9*, 323.
[6] Y. Rong, Y. Hu, A. Mei, H. Tan, M. I. Saidaminov, S. il Seok, M. D. McGehee, E. H. Sargent, H. Han, *Science* **2018**, *361*, eaat8235.
[7] D. Bryant, N. Aristidou, S. Pont, I. Sanchez-Molina, T. Chotchunangatchaval, S. Wheeler, J. R. Durrant Ab, S. A. Haque, *Energy Environ. Sci.* **2016**, *9*, 1655.
[8] G. Niu, W. Li, F. Meng, L. Wang, H. Dong, Y. Qiu, *J. Mater. Chem. A* **2014**, *2*, 705.
[9] A. K. Mishra, R. K. Shukla, **2020**, *29*, 836., https://doi.org/10.1016/j.matpr.2020.04.872.
[10] A. M. A. Leguy, Y. Hu, M. Campoy-Quiles, M. I. Alonso, O. J. Weber, P. Azarhoosh, M. van Schilfgaarde, M. T. Weller, T. Bein, J. Nelson, P. Docampo, P. R. F. Barnes, *Chem. Mater.* **2015**, *27*, 3397.
[11] S. Bae, S. Kim, S. W. Lee, K. J. Cho, S. Park, S. Lee, Y. Kang, H. S. Lee, D. Kim, *J. Phys. Chem. Lett.* **2016**, *7*, 3091.
[12] C. C. Boyd, R. Cheacharoen, T. Leijtens, M. D. McGehee, *Chem. Rev.* **2019**, *119*, 3418.
[13] E. M. Tennyson, T. A. S. Doherty, S. D. Stranks, **2019**, *4*, 573. https://doi.org/10.1038/s41578-019-0125-0.
[14] S. Ravishankar, A. Riquelme, S. K. Sarkar, M. Garcia-Batlle, G. Garcia-Belmonte, J. Bisquert, *J. Phys. Chem. C* **2019**, *123*, 24995.

[15] A. O. Alvarez, S. Ravishankar, F. Fabregat-Santiago, *Small Methods* **2021**, *5*, 2100661.
[16] T. A. Bull, L. S. C. Pingree, S. A. Jenekhe, D. S. Ginger, C. K. Luscombe, *ACS Nano* **2009**, *3*, 627.
[17] F. C. Krebs, R. Søndergaard, M. Jørgensen, *Sol. Energy Mater. Sol. Cells* **2011**, *95*, 1348.
[18] R. Rösch, D. M. Tanenbaum, M. Jørgensen, M. Seeland, M. Bärenklau, M. Hermenau, E. Voroshazi, M. T. Lloyd, Y. Galagan, B. Zimmermann, U. Würfel, M. Hösel, H. F. Dam, S. A. Gevorgyan, S. Kudret, W. Maes, L. Lutsen, D. Vanderzande, R. Andriessen, G. Teran-Escobar, M. Lira-Cantu, A. Rivaton, G. Y. Uzunoğlu, D. Germack, B. Andreasen, M. v. Madsen, K. Norrman, H. Hoppe, F. C. Krebs, *Energy Environ. Sci.* **2012**, *5*, 6521.
[19] S. Mastroianni, F. D. Heinz, J. Im, W. Veurman, M. Padilla, M. C. Schubert, U. Würfel, M. Grätzel, N. Park, A. C. Hinsch, *Nanoscale* **2015**, *7*, 19653.
[20] G. E. Eperon, D. Moerman, D. S. Ginger, *ACS Nano* **2016**, *10*, 10258.
[21] D. Yamashita, T. Handa, T. Ihara, H. Tahara, A. Shimazaki, A. Wakamiya, Y. Kanemitsu, *J. Phys. Chem. Lett.* **2016**, *7*, 3186.
[22] A. N. Jumabekov, E. della Gaspera, Z. Q. Xu, A. S. R. Chesman, J. van Embden, S. A. Bonke, Q. Bao, D. Vak, U. Bach, *J. Mater. Chem. C* **2016**, *4*, 3125.
[23] X. Lin, S. R. Raga, A. S. R. Chesman, Q. Ou, L. Jiang, Q. Bao, J. Lu, Y. B. Cheng, U. Bach, *Nano Energy* **2020**, *67*, 104223.
[24] Z. Song, A. Abate, S. C. Watthage, G. K. Liyanage, A. B. Phillips, U. Steiner, M. Graetzel, M. J. Heben, *Adv. Energy Mater.* **2016**, *6*, 1600846.
[25] Y. Yao, G. Wang, F. Wu, D. Liu, C. Lin, X. Rao, R. Wu, G. Zhou, Q. Song, *RSC Adv.* **2017**, *7*, 42973.
[26] L. Dloczik, O. Ileperuma, I. Lauermann, L. M. Peter, E. A. Ponomarev, G. Redmond, N. J. Shaw, I. Uhlendorf, *J. Phys. Chem. B* **1997**, *101*, 10281.
[27] J. Halme, *Phys. Chem. Chem. Phys.* **2011**, *13*, 12435.
[28] S. Ravishankar, C. Aranda, S. Sanchez, J. Bisquert, M. Saliba, G. Garcia-Belmonte, *J. Phys. Chem. C* **2019**, *123*, 6444.
[29] A. Bou, H. Ā Boliņš, A. Ashoka, H. Cruanyes, A. Guerrero, F. Deschler, J. Bisquert, *ACS Energy Lett.* **2021**, *6*, 2248.
[30] L. M. Peter, *Chem. Rev.* **1990**, *90*, 753.
[31] S. M. Sze, K. K. Ng, *Physics of Semiconductor Devices*, 3rd ed., Wiley, New York **2007**, 164.
[32] A. M. A. Leguy, P. Azarhoosh, M. I. Alonso, M. Campoy-Quiles, O. J. Weber, J. Yao, D. Bryant, M. T. Weller, J. Nelson, A. Walsh, M. van Schilfgaarde, P. R. F. Barnes, *Nanoscale* **2016**, *8*, 6317.
[33] P. Löper, M. Stuckelberger, B. Niesen, J. Jéré, J. Werner, M. Filipič, S.-J. Moon, J.-H. Yum, M. Topič, S. de Wolf, C. Ballif, *J. Phys. Chem. Lett.* **2015**, *6*, 66.
[34] A. Pockett, M. Spence, S. K. Thomas, D. Raptis, T. Watson, M. J. Carnie, *Sol. RRL* **2021**, *5*, 2100159.
[35] A. Pockett, G. E. Eperon, T. Peltola, H. J. Snaith, A. Walker, L. M. Peter, P. J. Cameron, *J. Phys. Chem. C* **2015**, *119*, 3456.
[36] A. Bou, A. Pockett, D. Raptis, T. Watson, M. J. Carnie, J. Bisquert, *J. Phys. Chem. Lett.* **2020**, *11*, 8654.
[37] S. D. Stranks, G. E. Eperon, G. Grancini, C. Menelaou, M. J. P. Alcocer, T. Leijtens, L. M. Herz, A. Petrozza, H. J. Snaith, *Science* **2013**, *342*, 341.
[38] Q. Dong, Y. Fang, Y. Shao, P. Mulligan, J. Qiu, L. Cao, J. Huang, *Science* **2015**, *347*, 967.
[39] J. Carstensen, G. Popkirov, J. Bahr, H. Föll, *Sol. Energy Mater. Sol. Cells* **2003**, *76*, 599.
[40] J. R. Sites, T. J. Nagle, in *Conf. Record of the IEEE Photovoltaic Specialists Conf*, IEEE, Lake Buena Vista, FL, USA **2005**, 199.
[41] B. Moralejo, M. A. González, J. Jiménez, V. Parra, O. Martínez, J. Gutiérrez, O. Charro, *J. Electron. Mater.* **2010**, *39*, 663.
[42] P. Vorasayan, T. R. Betts, R. Gottschalg, *Sol. Energy Mater. Sol. Cells* **2011**, *95*, 111.
[43] M. Acciarri, S. Binetti, A. Racz, S. Pizzini, G. Agostinelli, *Sol. Energy Mater. Sol. Cells* **2002**, *72*, 417.
[44] J. S. Laird, Y. Chen, L. Scheick, T. Vo, A. Johnston, *Rev. Sci. Instrum.* **2008**, *79*, 083705.
[45] J. S. Laird, B. C. Johnson, C. G. Ryan, *Meas. Sci. Technol.* **2012**, *23*, 085401.
[46] G. D. Tainter, M. T. Hörantner, L. M. Pazos-Outón, R. D. Lamboll, H. Āboliņš, T. Leijtens, S. Mahesh, R. H. Friend, H. J. Snaith, H. J. Joyce, F. Deschler, *Joule* **2019**, *3*, 1301.
[47] Y. Han, S. Meyer, Y. Dkhissi, K. Weber, J. M. Pringle, U. Bach, L. Spiccia, Y. B. Cheng, *J. Mater. Chem. A* **2015**, *3*, 8139.
[48] J. Barbé, M. Newman, S. Lilliu, V. Kumar, H. K. H. Lee, C. Charbonneau, C. Rodenburg, D. Lidzey, W. C. Tsoi, *J. Mater. Chem. A* **2018**, *6*, 23010.
[49] S. Ravishankar, M. Marisé Garcia-Batlle, J. Bisquert, G. Garcia-Belmonte, J. Odrobina, C.-A. Schiller, *J. Phys. Chem. C* **2020**, *124*, 15793.
[50] S. Ravishankar, C. Aranda, P. P. Boix, J. A. Anta, J. Bisquert, G. Garcia-Belmonte, *J. Phys. Chem. Lett.* **2018**, *9*, 3099.
[51] R. S. Sanchez, V. Gonzalez-Pedro, J. W. Lee, N. G. Park, Y. S. Kang, I. Mora-Sero, J. Bisquert, *J. Phys. Chem. Lett.* **2014**, *5*, 2357.
[52] R. Gottesman, E. Haltzi, L. Gouda, S. Tirosh, Y. Bouhadana, A. Zaban, E. Mosconi, F. de Angelis, *J. Phys. Chem. Lett.* **2014**, *5*, 2662.
[53] I. Zarazua, G. Han, P. P. Boix, S. Mhaisalkar, F. Fabregat-Santiago, I. Mora-Sero, J. Bisquert, G. G-Belmonte, *J. Phys. Chem. Lett.* **2016**, *7*, 5105.
[54] A. Singh, P. K. Nayak, S. Banerjee, Z. Wang, J. T. W. Wang, H. J. Snaith, K. S. Narayan, *Sol. RRL* **2018**, *2*, 1700173.
[55] A. Kumar, U. Bansode, S. Ogale, A. Rahman, *Nanotechnology* **2020**, *31*, 365403.
[56] S. Ravishankar, Z. Liu, U. Rau, T. Kirchartz, *PRX Energy* **2022**, *1*, 013003.
[57] W. Li, M. S. R. Huang, S. K. Yadavalli, J. D. Lizarazo Ferro, Y. Zhou, A. Zaslavsky, N. P. Padture, R. Zia, *ACS Photonics* **2019**, *6*, 2375.
[58] Y. Chen, H. T. Yi, X. Wu, R. Haroldson, Y. N. Gartstein, Y. I. Rodionov, K. S. Tikhonov, A. Zakhidov, X. Y. Zhu, V. Podzorov, *Nat. Commun.* **2016**, *7*, 12253.